

# Electric-Field-Induced Phase Transition in Mn-Doped (K<sub>0.48</sub>Na<sub>0.48</sub>Li<sub>0.04</sub>)NbO<sub>3</sub> Lead-Free Ceramics

H.E. Mgbemere<sup>\*1</sup>, G.A. Schneider<sup>2</sup>, L. Schmitt<sup>3</sup>, M. Hinterstein<sup>4</sup>

<sup>1</sup>Department of Metallurgical and Materials Engineering, University of Lagos, Lagos Nigeria

<sup>2</sup>Institute of Advanced Ceramics, Hamburg University of Technology,  
Denickestrasse 15, D-21073 Hamburg, Germany

<sup>3</sup>Material- und Geowissenschaften, Technische Universität Darmstadt, Darmstadt, Germany

<sup>4</sup>Institute for Applied Materials, Karlsruhe Institute for Technology, Karlsruhe, D-76131, Germany

received September 20, 2016; received in revised form November 7, 2016; accepted December 16, 2016

## Abstract

*In situ* applied-electric-field high-resolution X-ray diffraction has been used to study the field-induced response of Mn-doped (K<sub>0.48</sub>Na<sub>0.48</sub>Li<sub>0.04</sub>)NbO<sub>3</sub> (KNN-L) ceramics produced using the conventional mixed-oxide processing route. Ferroelectric domains are observed with transmission electron microscopy with indications of nano-segregation of Mn. Rietveld refinement (FULLPROF Suite) is used to refine the diffraction patterns, and a phase change from orthorhombic symmetry with space group *Amm*2 to tetragonal symmetry with space group *P4mm* is observed when the applied field exceeds 1.4 kV/mm. Phase coexistence between the two phases is also observed at applied fields between 1.2 kV/mm and 1.3 kV/mm with possible implications of being the coercive field  $E_C$  value of the sample. A better understanding of the structural behaviour of this type of lead-free ceramics will lead to improvements in their piezoelectric and electromechanical properties.

**Keywords:** (K<sub>x</sub>Na<sub>1-x</sub>)NbO<sub>3</sub>, high resolution, X-ray diffraction, electric field, lead-free ceramics

## I. Introduction

The need to replace the currently used but environmentally unfriendly lead-based piezoelectric ceramics has led to robust research on lead-free ceramic alternatives in the last couple of years. Of these classes of ferroelectric ceramics, (Bi<sub>0.5</sub>Na<sub>0.5</sub>)TiO<sub>3</sub> (BNT)-based<sup>1–4</sup> and (K<sub>x</sub>Na<sub>1-x</sub>)NbO<sub>3</sub> (KNN)<sup>5–9</sup> are among the most investigated.

Some of these lead-free piezoelectric ceramic compositions are now being tested for potential applications as ultrasonic transducers and the results show that very good electroacoustic performances comparable to those from commercial Pb(Zr<sub>x</sub>Ti<sub>1-x</sub>)O<sub>3</sub> ceramics have been obtained<sup>10–12</sup>. Poling at high temperatures as well as the formation of diffused phase transition is believed to result in an improved piezoelectric performance for CaZrO<sub>3</sub>-modified KNN-based ceramics<sup>13, 14</sup>.

The origin of the enhanced piezoelectric properties in these lead-free ceramics is not completely clear, since in some structural studies only small distortions are observed. This makes it necessary to investigate further with the help of *in situ* powder diffraction with an applied electric field<sup>3, 15</sup>. High-resolution diffraction techniques help to determine the crystallographic strain which can be used to compare with the results from the macroscopic strain. Due to the fact that phase transitions affect the dimensions

and symmetry of the unit cell, it should be observed from X-ray diffraction measurements and this technique has been used to study both lead-based and lead-free piezoelectric materials<sup>3, 16</sup>.

An *ab initio* based approach for PZT compositions near the morphotropic phase boundary (MPB) showed that applying electric field to the samples induced polarization paths. When the field was applied in <sup>111</sup> orientation, a transition from tetragonal to A-type monoclinic and finally to a rhombohedral structure is observed<sup>17</sup>. For a <001> oriented Pb(Mg<sub>1/3</sub>Nb<sub>2/3</sub>)O<sub>3</sub>-PbTiO<sub>3</sub> single crystal, the phase transition from monoclinic to tetragonal phase depends on temperature. The polarisation and longitudinal strain in the sample decreases in the range 23 °C – 75 °C<sup>18, 19</sup>. Phase transition from a pseudo-monoclinic structure to a tetragonal structure occurs with *in situ* X-ray diffraction for 0.92Pb(Zn<sub>1/3</sub>Nb<sub>2/3</sub>)O<sub>3</sub> – 0.08PbTiO<sub>3</sub> single crystal poled in the <001> direction. High crystallographic strains observed during the measurement using bulk techniques were ascribed to microscopic changes in the crystal lattice. We recently revealed the role of grain orientation on the electric-field-induced response in PZT-based actuator materials<sup>20</sup>, lead-free BNT-BT compositions<sup>21</sup> and incipient ferroelectrics<sup>22</sup> with powder diffraction.

A study of the effects of temperature and applied electric field on the structural modification of 0.95[0.94Bi<sub>0.5</sub>Na<sub>0.5</sub>TiO<sub>3</sub>–

\* Corresponding author: [hmgbemere@unilag.edu.ng](mailto:hmgbemere@unilag.edu.ng)

0.06BaTiO<sub>3</sub>] – 0.05K<sub>0.5</sub>Na<sub>0.5</sub>NbO<sub>3</sub> ceramics from 25 °C to 500 °C showed that in the unpoled sample, the rhombohedral phase content increases with increasing temperature<sup>23</sup>. An alternating-current-type electric field leads to reversible structural modifications that are necessary for the development of materials with improved energy storage properties. The electric-field-induced strain in 0.92Bi<sub>1/2</sub>Na<sub>1/2</sub>TiO<sub>3</sub> – 0.06BaTiO<sub>3</sub> – 0.02K<sub>1/2</sub>Na<sub>1/2</sub>NbO<sub>3</sub> using *in situ* synchrotron X-ray and neutron diffraction indicated that the tetragonal phase undergoes a reversible phase transition to a distorted rhombohedral phase. The large strain obtained is due to the reversible field-induced phase transformation from a nearly non-polar tetragonal phase to a ferroelectric active rhombohedral phase<sup>3</sup>. In single crystals of Mn-doped BNT-BT, there is a phase transition from rhombohedral to tetragonal symmetry when the electric field is applied in the [001] direction<sup>24</sup>. An electric field was used to transform the 0.94BNT-0.06BT ceramics from the near-cubic phase in the unpoled state to a predominantly rhombohedral structure with high lattice distortion and preferred orientation along the *c*-axis<sup>25</sup>. Temperature-dependent phase transition studies of KNN-L ceramics from 0 to 10 mol% Li revealed a series of phase changes from orthorhombic to tetragonal, while a secondary phase was observed with >7 mol% Li<sup>26</sup>. Inhomogeneities in the distribution of the alkali elements is also reported to occur for Li-modified KNN ceramics<sup>27</sup>.

*In situ* high-resolution X-ray diffraction with electric field application has been used to investigate the structural properties of our sample. The objective of this article is to study the structural evolution of the sample under the influence of an applied electric field.

## II. Materials and Methods

The starting powders for the synthesis are K<sub>2</sub>CO<sub>3</sub>, Na<sub>2</sub>CO<sub>3</sub>, Li<sub>2</sub>CO<sub>3</sub> (99+%), Nb<sub>2</sub>O<sub>5</sub> (99.9 %) (Chempur Feinchemikalien und Forschungs GmbH, Karlsruhe, Germany) and MnO<sub>2</sub> (99.5 %) (Merck Chemicals GmbH, Darmstadt, Germany). The powders were first dried in an oven to ensure that no moisture was present. Stoichiometric amounts of the raw powders were weighed in with a 2 % extra for the alkali-based carbonates. 2 mol% of Mn was introduced to the powders as MnO<sub>2</sub>. The powders were attrition-milled using ethanol as solvent, 3-mm zirconia balls as grinding media and a speed of 500 rpm for 2 h. The particle size analysis was carried out before, during and after milling to ensure that the average particle sizes of the powders were below 1 μm. The solvent (ethanol) was removed from the powder using a rotary evaporator while calcination was carried out for 4 h in a tube furnace operating at 850 °C with a heating rate of 3 °C/min. A second milling step was carried out to ensure powder homogeneity with sub-micron average particle size distribution. The powders were pressed in two steps: first with a uniaxial press operating at 75 MPa for 30 sec and subsequently with a cold isostatic press operating at 300 MPa for 2 min. The pellets were sintered at 1050 °C for 1 h in air atmosphere using a chamber furnace. The density of the samples was measured using the Archimedes method. Samples for hysteresis and diffrac-

tion were ground and polished in preparation for the measurements. The polarization hysteresis measurement was performed at room temperature using a standard Sawyer-Tower circuit with a complete dipolar measurement taking 200 sec while the unipolar strain hysteresis was done using a displacement transducer device inside a measurement kit containing silicon oil. Macroscopic strain values were calculated from the slope of the unipolar strain hysteresis curve. Samples for microstructure analysis were thermally etched at 900 °C for 30 min. Silver paints which enable electrical contact during the SEM measurement were applied on the top and side of the sample. Imaging was performed using the scanning electron microscope (FE-SEM Zeiss Supra 55 VP) while data acquisition was in the secondary electron mode. Details of the sample preparation steps for transmission electron microscope (TEM) image can be found elsewhere<sup>28</sup>. The grain size measurements were determined using the mean intercept length method from a minimum of six different areas of the micrograph. The high-resolution *in situ* electric-field-induced X-ray diffraction measurements were carried out at the Deutsches Elektronensynchrotron (DESY) radiation facility in Hamburg at beamline P02.1 of PETRA III at a photon energy of 60 keV ( $\lambda = 0.2073 \text{ \AA}$ ). All the data were collected with a Perkin Elmer 2D detector and radially integrated in 5° steps<sup>29,30</sup>. All the collected data were refined with the Rietveld method using FullProf suite<sup>31</sup>. Refinement of the background under the peaks was performed using linear interpolation between points from regions where no reflections had any contribution to the intensity. The model based on Thompson-Cox-Hastings pseudo-Voigt profile function<sup>32,33</sup> is used. Both the atomic positions and isotropic atomic displacement parameters  $B_{\text{iso}}$  were refined. Orthorhombic and tetragonal refinement models were used to extract information from the diffraction patterns. When a two-phase coexistence between the orthorhombic phase with space group *Amm2* and the tetragonal phase with space group *P4mm* was observed, a two-phase refinement model was used for the refinement. The amount of the constituent phases was calculated using the scale factors, which involves the product of mass and volume of the unit cell contents from each phase. The weight fraction of the phase was calculated using the equation below

$$W_p = \frac{S_p(Z, M, V)_p \cdot \tau_j}{\sum_j S_j(Z, M, V)_j \cdot \tau_p} \quad (1)$$

where  $W_p$  is the relative weight fraction of phase *p* in a mixture containing *j* phases while *S*, *Z*, *M* and *V* are the Rietveld scale factors from the refinement, number of formula units per cell, mass of formula unit and unit cell volume respectively. The phase-weighted lattice distortion in the sample is calculated as the summation of the product of the percentage of the phase present and the distortion of the phase. The crystallographic strain in the sample is calculated as the quotient of the change in lattice parameter after poling and the lattice parameter in the unpoled phase.

### III. Results

The scanning electron microscope image of the sample obtained using the secondary electron data acquisition mode is shown in Fig. 1a. Most of the grains in the micrograph are within the same size range and so a unimodal grain size distribution is used to analyse the grains. Large, isolated pores can also be observed at the grain boundaries and some of these pores may be due to grain pull-out during the grinding and polishing process. Different features (smooth and rough grains) inside the grains may be due to the different crystallographic planes inside the sample. The planes with higher energy try to revert to planes with lower energy and this may result in a stepped/rough surface. It could also be due to the ferroelectric domains in the sample. The calculated average grain size for the sample is  $8.2 \pm 3.2 \mu\text{m}$  while the value of the bulk density is  $4.19 \pm 0.05 \text{ g/cm}^3$

The bright field TEM image of the sample is shown in Fig. 1b. Ferroelectric domains which are predominantly of  $90^\circ$  orientation are observed in the image. Most of the surface is dark in appearance with an isolated spot with bright appearance. The energy dispersive spectroscopy

(EDX) spectrum carried out on the dark part of the TEM image is shown in Fig. 1c. The energy dispersive spectrum shows that there is very little or no manganese. Another EDX spectrum on the bright spot of the image is shown in Fig. 1d and shows a phase with Mn-rich exclusion ( $\sim 150 \text{ nm}$ ). This indicates that manganese in KNN ceramics has a tendency to segregate. Microsegregation of manganese in piezoelectric ceramics has been reported in the literature<sup>34, 35</sup>.

The plot of polarization hysteresis as a function of the electric field applied on the sample is shown in Fig. 2. During the measurement, there were indications that the sample was conductive and this could be observed by the shape of the graph. The value of the coercive field  $E_c$  for the sample ranges from  $0.9 \text{ kV/mm}$  to  $1.1 \text{ kV/mm}$  while the remnant polarisation  $P_r$  is  $\sim 17 \mu\text{C/cm}^2$ . The non-uniform nature of the hysteresis curve could be accounted for by an internal bias field in the sample that increases the mobility of the charge carriers which are believed to accumulate at the grain boundaries. Inhomogeneities in the distribution of the alkali elements, which has been reported for KNN-Li ceramics, is also believed to affect the polarisation response in the sample<sup>27</sup>.

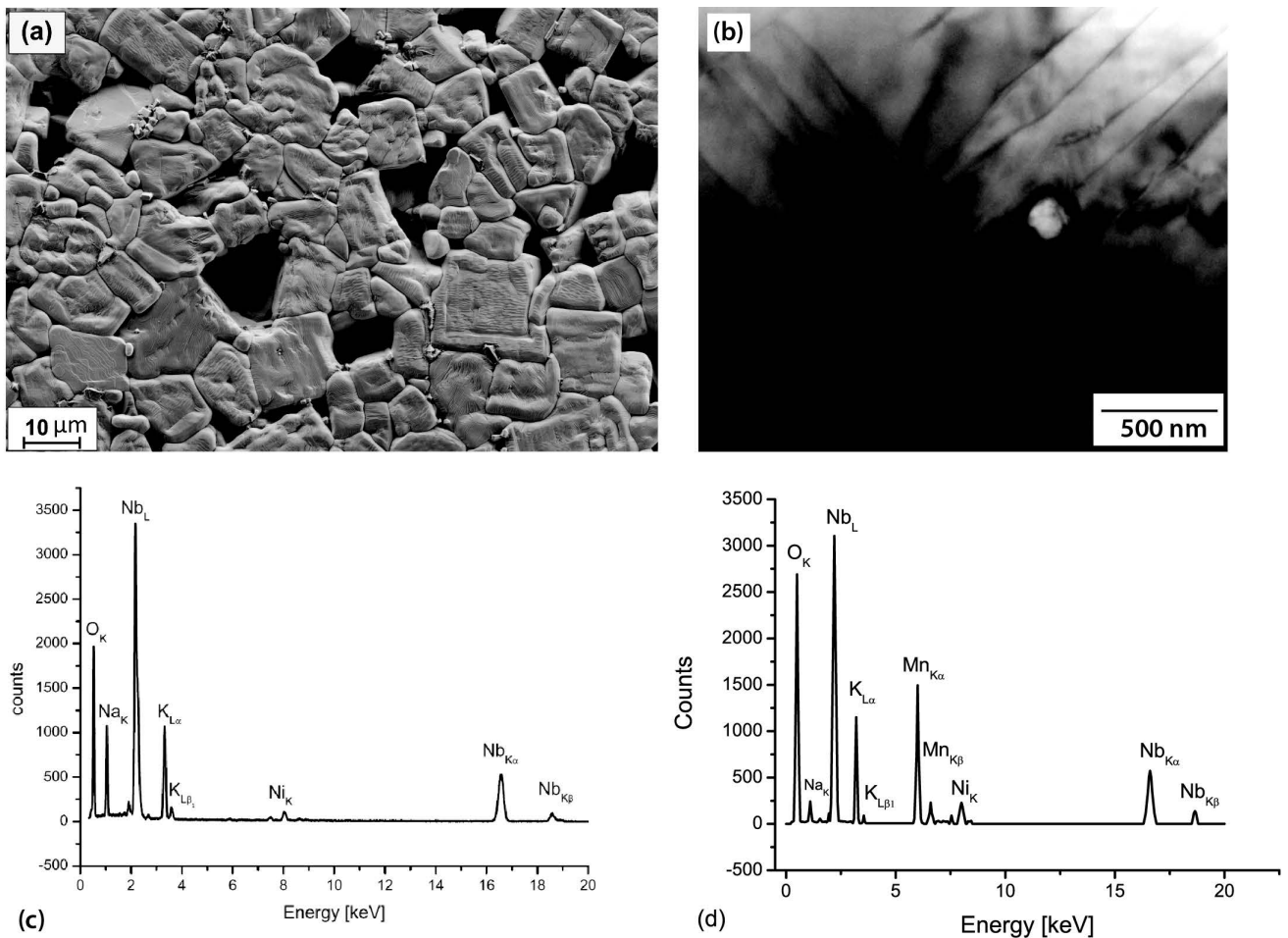


**Fig. 1:** (a) Scanning electron microscope (SEM) image of  $0.98(\text{K}_{0.48}\text{Na}_{0.48}\text{Li}_{0.04})\text{NbO}_3 - 0.02\text{MnO}_2$  ceramics, (b) Bright field Transmission Electron Microscope (TEM) image of  $0.98(\text{K}_{0.48}\text{Na}_{0.48}\text{Li}_{0.04})\text{NbO}_3 - 0.02\text{MnO}_2$  ceramics, (c) Energy dispersive spectroscopy of a section deficient in Mn and (d) Energy dispersive spectroscopy of a Mn-rich inclusion.

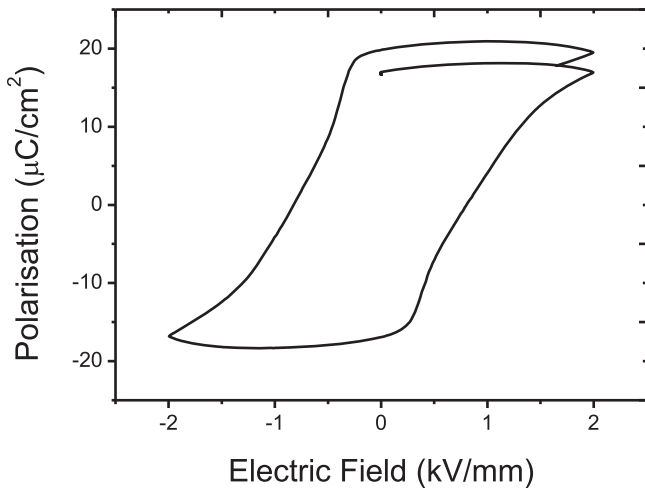


Fig. 2: A graph showing the variation of polarization against electric field for  $0.98(\text{K}_{0.48}\text{Na}_{0.48}\text{Li}_{0.04})\text{NbO}_3 - 0.02\text{MnO}_2$  ceramics at room temperature.

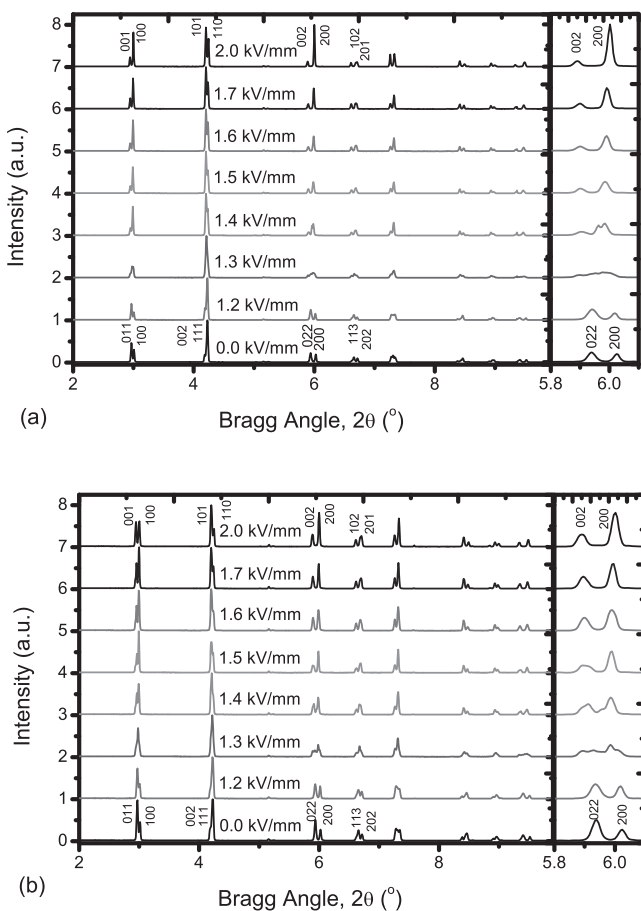


Fig. 3: *In situ* applied electric field high resolution X-ray diffraction patterns for (a)  $0.98(\text{K}_{0.48}\text{Na}_{0.48}\text{Li}_{0.04})\text{NbO}_3 - 0.02\text{MnO}_2$  ceramics where the angle of the viewing direction ( $\omega$ ) is  $0^\circ$  and (b) where the angle of the viewing direction is  $50^\circ$ . The inset on the right represents the pseudo-cubic 002 and 200 reflections showing the transition in phase present with increasing applied field.

The *in situ* high-resolution X-ray diffraction profiles for the sample with applied electric field are shown in Fig. 3. Two viewing directions are used to acquire the diffraction data and the effect of the angle of the viewing direction ( $\omega$ ) on the diffraction data are as shown in Figs. 3a and 3b respectively. With an applied field between 0 and 1.1 kV/mm, the diffraction patterns did not change con-

siderably and so the measurement at 0.0 kV/mm is used to represent them. The insets on the right are enlargements of the pseudo-cubic 002 and 200 reflections which show how the patterns change with increasing electric field. Poling and re-poling of piezoelectric materials used in electromechanical devices occur during the lifetime of these materials, and to have a glimpse into their behaviour under field, two poling cycles for the same sample was carried out. In the first poling cycle, a narrow range of phase coexistence is observed between fields of 1.3 and 1.4 kV/mm. There are occasions of dielectric breakdown during the measurement due to sample conductivity and possibly phase transition to the remanent phase. The large pores in the sample are believed to contribute to the lowering of the electrical resistance in the sample. The phase transition in the sample is from orthorhombic  $Amm2$  to tetragonal  $P4mm$  independent of the angle of viewing.

The *in situ* high-resolution X-ray diffraction data for the second poling cycle is shown in Fig. 4. With a 2 kV/mm electric field as in the first poling cycle, the diffraction pattern transforms to the tetragonal phase and when the field is removed, the diffraction pattern switches almost immediately to its initial state before application of the field. An abrupt phase transition from the orthorhombic  $Amm2$  phase to the tetragonal  $P4mm$  phase is observed with an applied field of 1.3 kV/mm.

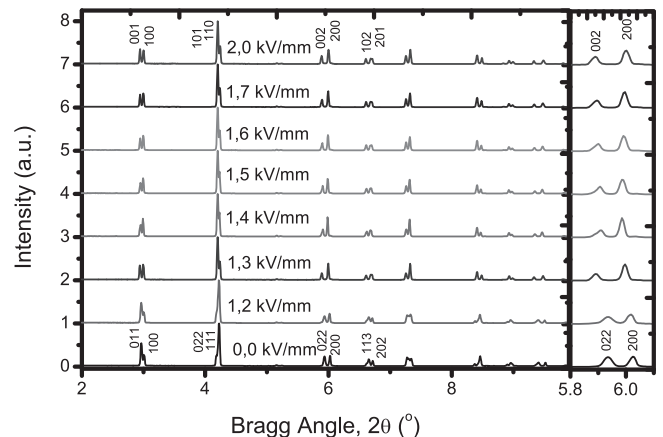
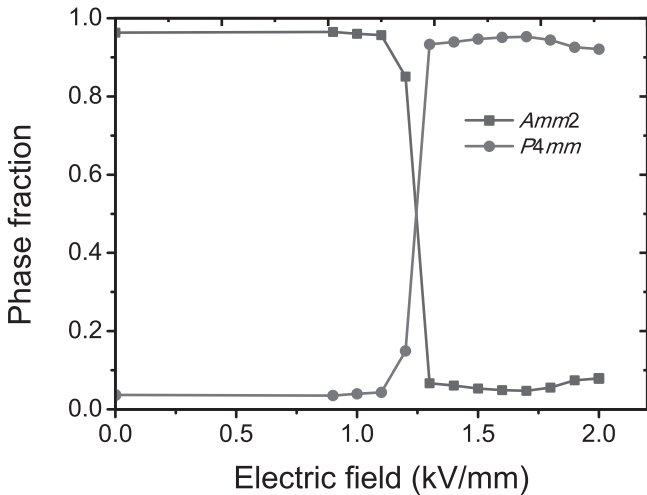


Fig. 4: Second poling cycle for *in situ* applied electric field high resolution X-ray diffraction patterns for  $0.98(\text{K}_{0.48}\text{Na}_{0.48}\text{Li}_{0.04})\text{NbO}_3 - 0.02\text{MnO}_2$  ceramics where the angle of the viewing direction ( $\omega$ ) is  $0^\circ$  deg. The inset on the right represents the pseudo-cubic 002 and 200 showing the transition in phase present with increasing applied field.

The graph of the phase fraction of the phases as a function of the applied field is shown in Fig. 5. With an applied electric field between 0 and 1.2 kV/mm, the orthorhombic phase with space group  $Amm2$  is present while between 1.3 and 1.4 kV/mm, a two-phase coexistence between the orthorhombic (0.85) and tetragonal (0.15) phase is observed. When the applied field is  $> 1.4$  kV/mm, the phase present is tetragonal with space group  $P4mm$ .

The plots of the phase-weighted lattice distortion ( $\eta$ ) and unit cell volume as a function of the applied field is shown in Fig. 6. The lattice distortion with applied field is low in the orthorhombic phase (0.008) and spikes at the phase transition region and remains high in the tetragonal phase (0.013–0.016). The unit cell volume also follows the same

trend by being low (~ 63.3 Å<sup>3</sup>) in the orthorhombic phase and spiking at the phase coexistence region before gradually returning to (~ 63.33 Å<sup>3</sup>) when the field is 2 kV/mm. The strong increase in both the lattice distortion and the unit cell volume at an applied field of 1.2 kV/mm could possibly correspond to the coercive field of the sample. Strong relaxation processes are also observed after the phase transition.



**Fig. 5:** A plot of the weight fraction of the phases as a function of the applied electric field for 0.98(K<sub>0.48</sub>Na<sub>0.48</sub>Li<sub>0.04</sub>)NbO<sub>3</sub> -0.02MnO<sub>2</sub> ceramics.

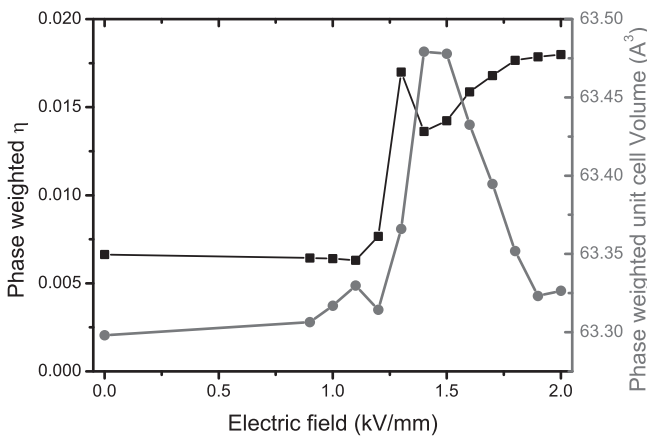
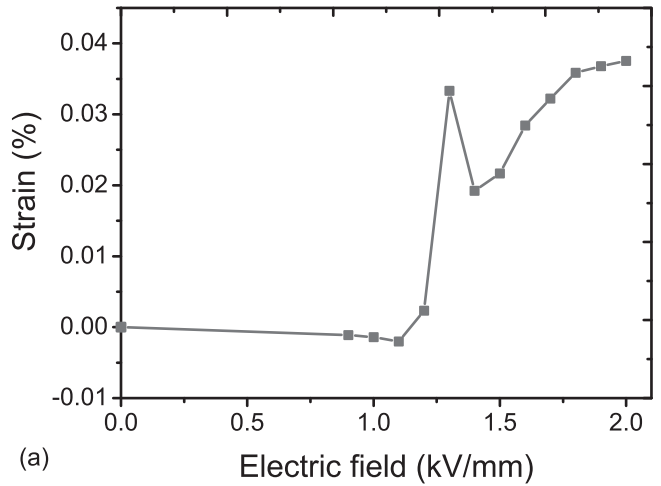


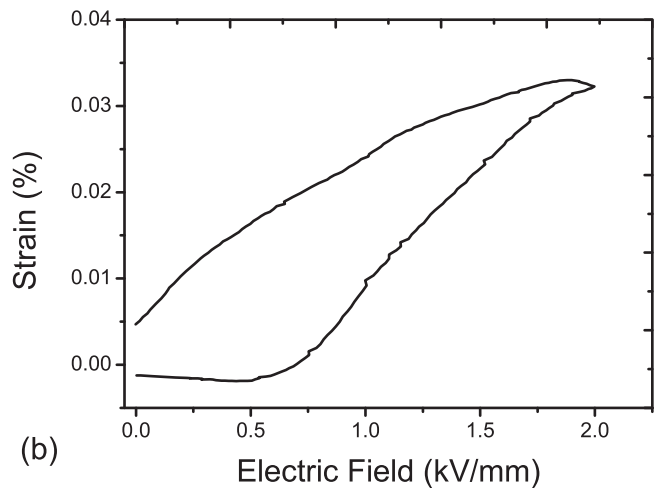
**Fig. 6:** A plot of the phase weighed lattice distortion  $\eta$  and the unit cell volume of 0.98(K<sub>0.48</sub>Na<sub>0.48</sub>Li<sub>0.04</sub>)NbO<sub>3</sub> -0.02MnO<sub>2</sub> ceramics as a function of the applied electric field.

The plots of the crystallographic strain and macroscopic strain obtained from unipolar strain hysteresis as a function of the applied electric field are shown in Figs. 7a and 7b respectively. The crystallographic strain in the sample in Fig. 7a is calculated from the lattice distortion  $\eta$  and the unit cell volume. In the crystallographic strain, the piezoelectric coefficient ( $d^*_{33}$ ) values are approximately 0 pm/V up to a field of 1.2 kV/mm and sharply rise to ~ 175 pm/V corresponding to the two-phase coexistence between 1.3 and 1.4 kV/mm. A small relaxation and later a gradual increase with field up to 200 pm/V at 2 kV/mm are observed. From the unipolar strain hysteresis measurement, with an applied field between 0 and 0.7 kV/mm, no strain values are obtained. This corresponds to the time and electric field required for the rearrangement of the crystallites to

the direction of the applied field. As the applied field increases, there is an almost linear increase in strain with a peak strain value of ~ 150 pm/V at 2 kV/mm. The difference in the two strain values is not very significant for samples with the same composition.



(a)



(b)

**Fig. 7:** Graph of (a) crystallographic strain and (b) macroscopic strain for 0.98(K<sub>0.48</sub>Na<sub>0.48</sub>Li<sub>0.04</sub>)NbO<sub>3</sub> -0.02MnO<sub>2</sub> ceramics as a function of the applied electric field.

**(1) Discussion**

The presence of large pores in the microstructure of piezoelectric ceramics affects their electromechanical properties through lowering of the density, dielectric properties, piezoelectric charge coefficients, etc. In the polarisation hysteresis measurement (Fig. 2) the shape of the hysteresis loop shows a deviation such that it could not close. A charge build-up occurs at the sample surface which results in a non-uniform field but is reduced near the sample centre when the field is applied. This deviation or non-linear behaviour of the piezoelectric effect in the sample depends on the direction of the electric field<sup>36</sup>.

Based only on the phase transformations resulting from the applied electric field, the coercive field of this sample could be estimated to be between 1.3 and 1.4 kV/mm. This value is lower than the coercive field for unpoled BNT ceramics which is ~ 2.2 kV/mm<sup>23</sup>.

The *in situ* electric-field-induced X-ray diffraction profiles indicate that there is a phase transition from an or-

thorhombic to a tetragonal phase. The jump in the lattice distortion and unit cell volume at the phase coexistence region could be due to polarisation rotation which increases the strain and polarisation leading to a discontinuous jump in both properties<sup>37</sup>. The jump in the crystallographic strain gives an indication that the polarisation rotation is not continuous i.e. it is a first order transition. The polarisation in the lattice can rotate continuously from  $[101]_C$  of the orthorhombic phase to the tetragonal  $[001]_C$  direction. In  $\text{BaTiO}_3$ , when a field-induced phase transition is observed, the polarisation rotates from the initial tetragonal  $[100]_C$  to orthorhombic  $[110]_C$  direction<sup>38</sup>. This phase change from orthorhombic to tetragonal indicates that there is  $90^\circ$  domain switching from 200 to 002 orientation<sup>36</sup> while residual stresses are also important in the switching and phase change of non- $180^\circ$  domains.

When the electric field is removed, the intensity of the peak decreases and only the remanent strain remains in the sample. It is possible that a path switch takes place when there is a large piezoelectric response<sup>17</sup>. The degree of phase transition can be determined by the intensity of the poling field and the history of poling in the sample<sup>39</sup>. In the unpoled sample, as the field is applied, a pronounced effect on the diffraction profile is observed while the effect of a second application to the same sample was less pronounced. The microscopic strain closely matches the macroscopic strain measurement as seen in Fig. 7.

#### IV. Conclusions

*In situ* X-ray diffraction with applied electric field has been used to induce a phase transition in  $0.98(\text{K}_{0.48}\text{Na}_{0.48}\text{Li}_{0.04})\text{NbO}_3 - 0.02\text{MnO}_2$  piezoelectric ceramics. The changes in the X-ray diffraction profiles indicate that domains in the samples can be switched when an electric field is applied. Residual stresses are very important in inducing domain switching and phase change. A reversible field-induced phase transition from orthorhombic  $Amm2$  to tetragonal  $P4mm$  has been observed with this transition being independent of the viewing direction. There were occasions of breakdown of field due to conductivity and phase transition to the remanent phase. The strain mechanism in the sample appears to be mainly dependent on the unit cell volume. A better understanding of the structural evolution of the phases as the electric field is being applied has been elucidated. The result of this study can be used to estimate the behaviour of other KNN-based ceramics when they are subjected to applied electric fields. This result is important for future research in the sense that it will give other people insight into improving the electromechanical properties of lead-free piezoelectric ceramics.

#### Acknowledgement

This work was supported by the Deutsche Forschungsgemeinschaft (DFG) (Grant: SCHN 372/16–2 and HI 1867/1–1) and the University of Lagos (Grant: CRC NO. 2016/14). Access to use the beamline P02.1 at PETRA III at the DESY facility in Hamburg, Germany is greatly appreciated.

#### References

- 1 Takenaka, T., Sakata, K.: Dielectric, piezoelectric and pyroelectric properties of  $(\text{BiNa})_{1/2}\text{TiO}_3$ -based ceramics, *Ferroelectrics*, **95**, 153–156, (1989).
- 2 Lu, Y., Li, Y., Wang, D., Wang, T., Yin, Q.: Lead-free piezoelectric ceramics of  $(\text{Bi}_{1/2}\text{Na}_{1/2})\text{TiO}_3$ - $(\text{Bi}_{1/2}\text{K}_{1/2})\text{TiO}_3$ - $(\text{Bi}_{1/2}\text{Ag}_{1/2})\text{TiO}_3$  system, *J. Electroceramic*, **21**, 309–313, (2008).
- 3 Hinterstein, M., Knapp, M., Hoelzel, M., Jo, W., Cervellino, A., Ehrenberg, H., Fuess, H.: Field-induced phase transition in  $\text{Bi}_{1/2}\text{Na}_{1/2}\text{TiO}_3$ -based lead-free piezoelectric ceramics, *J. Appl. Cryst.*, **43**, 1314–1321, (2010).
- 4 Picht, G., Toepfer, J., Hennig, E.: Structural properties of  $(\text{Bi}_{0.5}\text{Na}_{0.5})_{1-x}\text{Ba}_x\text{TiO}_3$  lead-free piezoelectric ceramics, *J. Eur. Ceram. Soc.*, **30**, 3445–3453, (2010).
- 5 Egerton, L., Dillion, D.M.: Piezoelectric and dielectric properties of ceramics in the system potassium-sodium niobate, *J. Am. Ceram. Soc.*, **42**, 438–442, (1959).
- 6 Guo, Y., Kakimoto, K.-I., Ohsato, H.:  $(\text{Na}_{0.5}\text{K}_{0.5})\text{NbO}_3$  -  $\text{LiTaO}_3$  lead-free piezoelectric ceramics, *Mater. Lett.*, **59**, 241–244, (2005).
- 7 Matsubara, M., Yamaguchi, T., Kikuta, K., Shin-Ichi, H.: Effect of li substitution on the piezoelectric properties of potassium sodium niobate ceramics, *Jpn. J. Appl. Phys.*, **44**, 6136–6142, (2005).
- 8 Mgbemere, H.E., Hinterstein, M., Schneider, G.A.: Electrical and structural characterization of  $(\text{K}_x\text{Na}_{1-x})\text{NbO}_3$  ceramics modified with li and ta, *J. Appl. Cryst.*, **44**, 1080–1089, (2011).
- 9 Wang, L., Ren, W., Ma, W., Liu, M., Shi, P., Wu, X.: Improved electrical properties for Mn-doped lead-free piezoelectric potassium sodium niobate ceramics, *AIP Advances*, **5**, 097120, (2015).
- 10 Edwards, G.C., Choy, S.H., Chan, H.L.W., Scott, D.A., Batten, A.: Lead-free transducer for non-destructive evaluation, *Appl. Phys. A*, **88**, 209–215, (2007).
- 11 Bah, M., Giovannelli, F., Schoenestein, F., Brosseau, C., Deschamps, J.-R., Dorvaux, F., Haumesser, L., Clezi, E.L., Monot-Laffez, I.: Ultrasonic transducers based on undoped lead-free  $(\text{K}_{0.5}\text{Na}_{0.5})\text{NbO}_3$  ceramics, *Ultrasonics*, **63**, 23–30, (2015)
- 12 Wang, X., Wu, J., Xiao, D., Zhu, J., Cheng, X., Zheng, T., Zhang, B., Lou, X., Wang, X.: Giant piezoelectricity in Potassium-Sodium niobate lead-free ceramics, *J. Am. Chem. Soc.*, **136**, 2905–2910, (2014).
- 13 Yao F.-Z., Wang, K., Jo, W., Lee, J.-S., Li, J.-F.: Effect of poling temperature on piezoelectricity of  $\text{CaZrO}_3$ -modified  $(\text{K}, \text{Na})\text{NbO}_3$ -based lead-free ceramics, *J. Appl. Phys.*, **116**, 114102:1–6, (2014).
- 14 Yao, F.-Z., Wang, K., Jo, W., Webber, K.G., Comyn, T.P., Ding, J.-X., Xu, B., Cheng, L.-Q., Zheng, M.-P., Hou, Y.-D., Li, J.-F.: Diffused phase transition boosts thermal stability of high-performance lead-free piezoelectrics, *Adv. Funct. Mater.*, **26**, 1217–1224, (2016).
- 15 Schoenau, K.A., Schmitt, L.A., Knapp, M., Fuess, H., Eichel, R.-A., Kungl, H., Hoffmann, M.J.: Nanodomain structure of  $\text{Pb}(\text{Zr}_{1-x}\text{Ti}_x)\text{O}_3$  at its morphotropic phase boundary: investigations from local to average structure, *Phys. Rev. B*, **75**, (2007).
- 16 Durbin, M.K., Jacobs, E.W., Hicks, J.C., Park, S.-E.: *In situ* x-ray diffraction study of an electric field induced phase transition in the single crystal relaxor ferroelectric, 92%  $\text{Pb}(\text{Zr}_{1/3}\text{Nb}_{2/3})\text{O}_3$ -8%  $\text{PbTiO}_3$ , *Appl. Phys. Lett.*, **74**, 2848–2850, (1999).
- 17 Bellaiche, L., Garcia, A., Vanderbilt, D.: Electric-field induced polarization paths in  $\text{Pb}(\text{Zr}_{1-x}\text{Ti}_x)\text{O}_3$  alloys, *Condensed Matter- Materials Science*, *arXiv: cond-mat/0104335*, 1–4 (2001)

- 18 Ren, W., Han, L., Wicks, R., Yang, G., Mukherjee, B.K.: Electric-field-induced phase transitions of <001>-oriented Pb(Mg<sub>1/3</sub>Nb<sub>2/3</sub>)O<sub>3</sub>-PbTiO<sub>3</sub> single crystals, In: *Smart Structures and Materials 2005: Active Materials: Behavior and Mechanics*, Bellingham, WA, 272–278 (2005).
- 19 Chien, R.R., Tu, C.-S., Schmidt, V.H., Wang, F.-T.: Electric-field-induced and temperature-induced phase transitions in high-strain ferroelectric Pb(Mg<sub>1/3</sub>Nb<sub>2/3</sub>)<sub>0.67</sub>Ti<sub>0.33</sub>O<sub>3</sub> single crystal, *J. Phys.: Condens. Matter*, **18**, 8337–8344, (2016).
- 20 Hinterstein, M., Hoelzel, M., Rouquette, J., Haines, J., Glaum, J., Kungl, H., Hoffman, M.: Interplay of strain mechanisms in morphotropic piezoceramics, *Acta Mater.*, **94**, 319–327, (2015).
- 21 Hinterstein, M., Schmitt, L.A., Hoelzel, M., Jo, W., Rödel, J., Kleebe, H.-J., Hoffman, M.: Cyclic electric field response of morphotropic Bi<sub>1/2</sub>Na<sub>1/2</sub>TiO<sub>3</sub>-BaTiO<sub>3</sub> piezoceramics, *Appl. Phys. Lett.*, **106**, 222904, (2015).
- 22 Acosta, M., Schmitt, L., Cazorla, A.C., Studer, A., Zintler, A., Glaum, J., Kleebe, H.J., Donner, W., Hoffman, M., Rödel, J., Hinterstein, M.: Piezoelectricity and rotostriction through polar and non-polar coupled instabilities in bismuth-based piezoceramics., *Sci Rep.*, **6**, 28742, (2016).
- 23 Viola, G., Ning, H., Reece, M.J., Wilson, R., Correia, T.M., Weaver, P., Cain, M.G., Yan, H.: Reversibility in electric field-induced transitions and energy storage properties of bismuth-based perovskite ceramics, *J. Phys. D: Appl. Phys.*, **45**, 1–7, (2012).
- 24 Ge, W., Li, J., Viehland, D., Luo, H.: Influence of mn doping on the structure and properties of Na<sub>0.5</sub>Bi<sub>0.5</sub>TiO<sub>3</sub> single crystals, *J. Am. Ceram. Soc.*, **93**, 1372–1377, (2010)
- 25 Simons, H., Daniels, J., Jo, W., Dittmer, R., Studer, A., Avdeev, M., Rödel, J., Hoffman, M.: Electric-field-induced strain mechanisms in lead-free 94%(Bi<sub>1/2</sub>Na<sub>1/2</sub>)TiO<sub>3</sub>-6%BaTiO<sub>3</sub>, *Appl. Phys. Lett.*, **98**, 1–4, (2011).
- 26 Klein, N., Hollenstein, E., Damjanovic, D., Trodahl, H.J., Setter, N.: A study of the phase diagram of (K,Na,Li)NbO<sub>3</sub> determined by dielectric and piezoelectric measurements, and raman spectroscopy, *J. Appl. Phys.*, **102**, 014112, (2007).
- 27 Cheng, L.-Q., Wang, K., Yao, F.-Z., Zhu, F., Li, J.-F.: Composition inhomogeneity due to alkaline volatilization in li-modified (K, Na)NbO<sub>3</sub> lead-free piezoceramics, *J. Am. Ceram. Soc.*, **96**, 2693–2695, (2013).
- 28 Schmitt, L.A., Hinterstein, M., Kleebe, H.-J., Fuess, H.: Comparative study of two lead-free piezoceramics using diffraction techniques, *J. Appl. Cryst.*, **43**, 805–810, (2010).
- 29 Dippel, A.-C., Liermann, H.-P., Delitz, J.T., Walter, P., Schulte-Schrepping, H., Seeck, O.H., Franz, H.: Beamline P02.1 at PETRA III for high-resolution and high-energy powder diffraction, *J. Synchrotron. Rad.*, **22**, 1–4, (2015).
- 30 Herklotz, M., Scheiba, F., Hinterstein, M., Nikolowski, K., Knapp, M., Dippel, A.-C., Giebeler, L., Eckert, J., Ehrenberg, H.: Advances in *in situ* powder diffraction of battery materials: a case study of the new beamline P02.1 at DESY, hamburg, *J. Appl. Cryst.*, **46**, 1117–1127, (2013).
- 31 Rodríguez-Carvajal, J.: Recent advances in magnetic structure determination by neutron powder diffraction, *Physica B: Condensed Matter*, **192**, 55–69, (1993).
- 32 Hastings, J.B., Thomlinson, W., Cox, D.E.: Synchrotron X-ray powder diffraction, *J. Appl. Cryst.*, **17**, 85–95, (1984).
- 33 Finger, L. W., Cox, D.E., Jephcoat, A.P.: A correction for powder diffraction peak asymmetry due to axial divergence, *J. Appl. Cryst.*, **27** 892–900 (1994)
- 34 Olsen, G.H.: Texturing of lead-free piezoelectric ceramics, In: *Department of Materials Science and Engineering*. Master of Science Trondheim: Norwegian University of Science and Technology, 1–96, 2012.
- 35 Bah, M., Giovannelli, F., Retoux, R., Bustillo, J., Clezio, E.L., Monot-Laffez, I.: Crystal growth and piezoelectric properties of Lead-free based K<sub>0.5</sub>Na<sub>0.5</sub>NbO<sub>3</sub> by the floating zone method, *Cryst. Growth Des.*, **16**, 315–324, (2016).
- 36 Liu, M., Hsia, K.J., Jr., M.S.: In situ X-ray diffraction study of electric field induced domain switching and phase transition in PZT-5H, *J. Am. Ceram. Soc.*, **88**, 210–215, (2005).
- 37 Davis, M., Damjanovic, D., Setter, N.: Electric-field-, temperature-, and stress-induced phase transitions in relaxor ferroelectric single crystals, *Phys. Rev. B*, **73**, 014115:1–16, (2006).
- 38 Franzbach, D.J. Gu, Y.J., Chen, L.Q., Webber, K.G.: Electric field-induced tetragonal to orthorhombic phase transitions in [110]<sub>c</sub>-oriented BaTiO<sub>3</sub> single crystals, *Appl. Phys. Lett.*, **101**, 232904:1–4, (2012).
- 39 Chen, W., Lynch, C.S.: A Micro-electro-mechanical model for polarisation switching of ferroelectric materials, *Acta. Mater.*, **46**, 5303–5311, (1998).

